# Velocity Spectrum Estimation in Shock-Wave/Turbulent Boundary-Layer Interaction

Tetyana Jiang*
*Centre National d'Etudes Spatiales, 75612 Paris, France*
Anne-Marie Schreyer†
*TU Braunschweig, 38109 Braunschweig, Germany*
and
Lionel Larchevêque,‡ Sébastien Piponniau,‡ and Pierre Dupont§
*Aix-Marseille University, 13331 Marseille, France*

DOI: 10.2514/1.J055811

**The present paper presents the application of a technique to estimate velocity spectra on the complex supersonic flowfield of a shock-wave/turbulent boundary-layer interaction. A combined numerical–experimental approach relying on dual particle image velocimetry measurements and large-eddy simulations is used to optimize and validate a method allowing the reconstruction of spectral quantities from cross-correlations sampled at an arbitrary low sampling frequency from a Taylor-like hypothesis. The method, previously applied to a slowly streamwise developing boundary-layer flow, is refined so as to be able to better cope with flows having a higher degree of inhomogeneity. The accuracy and robustness of the resulting spectral estimates are evaluated in various characteristic regions distributed over the whole shock-wave/turbulent boundary-layer interaction flowfield thanks to the long-time large-eddy simulation database. Metrics allowing an a priori evaluation of the accuracy are also derived. Velocity spectra are then obtained from the experiments for the same locations. Comparisons with their large-eddy simulation counterparts make it possible to gain some insights into the origin of differences found between the experiments and the numerical simulation.**

## Nomenclature

$L$ = interaction length
$M_\infty$ = upstream Mach number
$p_0$ = stagnation pressure
$R$ = correlation function
$r$ = correlation coefficient
$r^L$ = Lagrangian correlation coefficient
$T_0$ = stagnation temperature
$U_\infty$ = upstream external velocity
$u$ = streamwise velocity component
$w^S$ = space weighting
$w^T$ = time weighting
$\boldsymbol{x}$ = position vector
$x$ = streamwise coordinate
$y$ = wall-normal coordinate
$y^+$ = altitude in wall unit
$\alpha$ = deviation angle of the incident shock
$\delta_{99}$ = boundary-layer thickness
$\Theta_k$ = set of discrete time delays
$\boldsymbol{\xi}$ = space distance vector
$\tau$ = time delay
$\tau_i$ = discrete time delay
$\langle\cdot\rangle$ = time-averaging operator

*Subscripts*

$c$ = convection
int = interpolated

## I. Introduction

SHOCK-WAVE/TURBULENT boundary-layer interactions occur in a large number of aerospace engineering applications with supersonic flow, such as rocket engine nozzles, supersonic and hypersonic vehicles, and airbreathing engine intakes. The flowfield of a shock-wave/turbulent boundary-layer interaction is highly unsteady, and the spatiotemporal development of the flow (as well as the characteristic frequency domain) is of great interest to gain a deeper understanding of the flowfield and ultimately to allow for more efficient engine and vehicle designs. The flowfield that we intend to investigate, a reflected plane–shock interaction at Mach 2, has a large range of characteristic frequencies between O(100 Hz) ($St_{\delta_{99}} = \mathrm{O}(2 \times 10^{-3})$) for the shock motion and breathing pulsations of the separation bubble, O(10–50 kHz) ($St_{\delta_{99}} = \mathrm{O}(0.2\text{–}0.5)$) for the incoming boundary layer, and O(100 kHz) ($St_{\delta_{99}} = \mathrm{O}(2)$) for the turbulent microscales [1].

Particle image velocimetry (PIV) provides the velocity field in one entire plane, but, to our knowledge, no time-resolved systems able to cover such a wide range of frequencies with accurate spatial resolution exist yet. With our newly developed dual-PIV system [2], certain temporal information can be obtained from the chosen temporal delay between the two systems: two independent PIV systems are observing the same field of view. Because of careful synchronization of the systems, two consecutive PIV velocity fields at arbitrarily small temporal delays can be obtained with the same spatial resolution as for standard PIV systems of high quality. However, to obtain complete spectral information, a very large number of measurements at a wide range of different temporal delays have to be performed, which means excessive experimental effort and costs.

Therefore, Schreyer et al. [3] suggested a method using the spatiotemporal information contained in the dual-PIV measurements to reconstruct temporal autocorrelations from spatial cross-correlations determined at each of the temporal delays $\delta\tau$ of the systems for which measurements were realized. To do so, the convection velocity of boundary-layer structures is taken into account, similar to Taylor's hypothesis. For regions in the flowfield that are convection-dominated, temporal correlations can then be reconstructed at time delays $\delta\tau_i$ that slightly differ from the measurement time delays $\delta\tau$. Of course, the time delays $\delta\tau$ for which

---

Received 31 October 2016; revision received 8 April 2017; accepted for publication 25 May 2017; published online 11 August 2017.

*Postdoctoral Research Fellow, DLA; currently IUSTI, UMR CNRS 7343, 13013 Marseille, France.

†Postdoctoral Research Fellow, Institute of Fluid Mechanics.

‡Associate Professor, IUSTI UMR CNRS 7343.

§Senior Scientist, IUSTI, UMR CNRS 7343.

measurements are performed have to be chosen sensibly to obtain a realistic reconstruction.

The method was applied and tested on a supersonic turbulent boundary layer in a combined experimental–numerical approach [3]. Numerical simulation data of a Mach 2 turbulent boundary layer from large-eddy simulation (LES) and dual-PIV measurements of the same boundary layer were used to show the suitability of the approach in complex supersonic flows. Furthermore, this combined experimental–numerical approach offers the means to test the possibilities and limitations of the method as well as to determine sensible parameters for the measurements. In this paper, we applied the approach to PIV measurements in a Mach 2 reflected shock interaction, and results will be shown of reconstructed spectra in a number of selected locations throughout the interaction, along with a discussion of the physics of the flowfield.

The contents of this paper are the following. In Sec. II, the idea and principle of the reconstruction method are presented. Section III describes the experimental and numerical setups, including the measurement principle of the dual-PIV system with which we collect the data on which the reconstruction method will be applied, the numerical setup for the shock-wave/boundary-layer interaction study, and some elements of validation for the computations. The evaluation of the method for the interaction flowfield is presented in Sec. IV, and several metrics for estimating the accuracy of the reconstruction method from available data are proposed. The results of the application of the method on dual-PIV data are then presented in Sec. V. Conclusions follow in Sec. VI.

## II. Principle of the Reconstruction Method

Assuming that dual-PIV measurements are available for a small number $n$ of time delays $\tau_i$, $i = 1, \ldots, n$, the cross-correlation function of the velocity $R(\boldsymbol{x}, \xi, \tau)$ between a reference location $\boldsymbol{x}$ and in its vicinity, defined by

$$R(\boldsymbol{x}, \boldsymbol{\xi}, \tau) = \langle u(\boldsymbol{x}, t) u(\boldsymbol{x} - \boldsymbol{\xi}, t - \tau) \rangle - \langle u(\boldsymbol{x}, t) \rangle \times \langle u(\boldsymbol{x} - \boldsymbol{\xi}, t - \tau) \rangle \tag{1}$$

as well as the cross-correlation coefficient $r(\boldsymbol{x}, \boldsymbol{\xi}, \tau)$, can be computed for both positive and negative time delays $\pm\tau_i$ using the time-average operator $\langle \cdot \rangle$.

The power spectra of the velocity estimated, following Blackman and Tukey [4], by computing the time Fourier transform of the autocorrelation $R(\boldsymbol{x}, 0, \tau)$ will, however, yield very poor bandwidth and/or spectral resolution because of the low values of $n$ compatible with realistically feasible experimental efforts for dual-PIV.

The basic idea of the method described in Schreyer et al. [3] is to take advantage of the cross-correlation information in space made available by the dual-PIV by assuming a convection-dominated flow and then considering the convected frame of reference to interpolate the autocorrelation function between consecutive known values at $\tau_i$ and $\tau_{i+1}$. This is conceptually similar the Taylor hypothesis, but the convection assumption is invoked over short time intervals $[\tau_i, \tau_{i+1}]$ rather than up to the maximum lag time as in standard approaches. The displacement associated with the convection is estimated from the dual-PIV data by seeking for every $\tau_i$ the separation distance $\xi_i$ for which the cross-correlation coefficient is maximum. Such values of the cross-correlation coefficient are formally similar to values of the Lagrangian autocorrelation coefficient $r^L(\boldsymbol{x}, \tau)$.

In the aforementioned [3], in which a boundary-layer flow was considered, the displacement of the reference frame was modeled as being directly proportional to $\tau$, with distinct proportionality constants (i.e., convection velocities) for the $\tau \leq 0$ and $\tau \geq 0$ regions. The proportionality constants were computed by performing a linear regression on the $(\boldsymbol{x} - \boldsymbol{\xi}_i, \tau_i)$ data set restricted to the $m$ lag times for which the approximated Lagrangian autocorrelation coefficient is above a given threshold.

This approximation scheme has been refined in the present work to possibly better deal with the higher degree of inhomogeneity found in the flow under consideration. A smoothed piecewise linear approximation is obtained from the same restricted $(\boldsymbol{x} - \boldsymbol{\xi}_i, \tau_i)$ data set of size $m$ by blending through Hermite interpolation over $[\tau_i, \tau_{i+1}]$ two affine estimates computed by least-square fittings over intervals $j = (i - 1, i, 1 + 1)$ and $j = (i, i + 1, i + 2)$, respectively. Boundary conditions for $\tau = \tau_1 = 0$ and $\tau = \tau_m$ are obtained by considering respectively a linear fitting over $[-\tau_2, \tau_2]$ and an affine fitting over $[\tau_{m-2}, \tau_m]$. If $m$ is lower than 3, the displacement is simply estimated from the original scheme.

Convection paths estimated from the original and new schemes in two regions of high streamline curvatures are plotted in Fig. 1a. The upper plot corresponds to a region located above the apex of the separation bubble, in which vortices coming from the oblique mixing layer developing over the upstream half of the bubble ($\xi > 0$) are shed downstream almost horizontally. Both schemes describe similarly the displacement along the mixing layer, but the progressive downturn for $\xi > 0$ is better captured by the new scheme. The ability of the new scheme to better deal with deflections encountered in inhomogeneous flows is also evidenced on the lower plot, corresponding to a point located in the last third of the separation bubble for which the streamline has a vertical tangent.

Once the convection path has been approximated, the value of the autocorrelation coefficient for $\tau \in [\tau_i, \tau_{i+1}]$ can then be estimated by considering the cross-correlation coefficients for $\tau_i$ and $\tau_{i+1}$ at suitable locations deduced from the convection hypothesis. The estimation process is sketched in Fig. 1b, where a one-dimensional convection is considered for the sake of simplicity. Two further estimates can be obtained from lag times $-\tau_{i+1}$ and $-\tau_i$ by taking advantage of the evenness of the autocorrelation coefficient. The four estimates are then weighted to obtain the final interpolation of the autocorrelation coefficient.

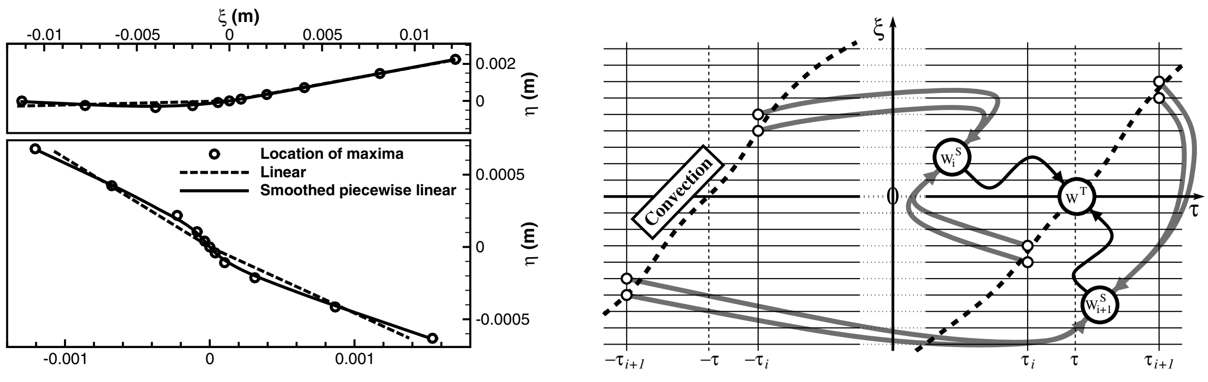

**a) Approximation of the convection above the apex of the separation bubble (top) and within the separation bubble (bottom)**

**b) Interpolation from the cross-correlation by trading space for time**

**Fig. 1 Schematic of the reconstruction method.**

Estimates obtained respectively from the time delays $\pm\tau_i$ and $\pm\tau_{i+1}$ are linearly weighted in time based on the relative time using the function

$$w^T(\tau) = (\tau - \tau_i)/(\tau_{i+1} - \tau_i) \tag{2}$$

In Schreyer et al. [3], the upstream/downstream estimates for time delay $\pm\tau_i$ (respectively $\pm\tau_{i+1}$) were simply averaged because upstream and downstream convection were statistically similar because of the quasi homogeneity of a boundary-layer flow in the streamwise direction.

For the present shock-wave/boundary-layer interaction, upstream and downstream convection processes can significantly differ in direction, as seen in Fig. 1a, but also in integral time scale. As a consequence, the reliability of the upstream/downstream estimates can differ, as quantified by the value of the Lagrangian autocorrelation coefficients. A space weighting between upstream and downstream estimates is therefore desirable; it is achieved by considering for a given $\tau \in [\tau_i, \tau_{i+1}]$ the interpolated value $r^L_{\mathrm{int}}$ of the Lagrangian correlation coefficient through a cubic natural spline (a null second derivative is imposed at boundaries $\pm\tau_m$). Several definitions of the space weighting $w^S$ have been tested using the LES databases of an $M = 2$ supersonic boundary layer; the one yielding the best compromise between accuracy and robustness reads

$$w^S_i(\tau) = \frac{[r^L_{\mathrm{int}}(\boldsymbol{x}, \tau - \tau_i)]^4}{[r^L_{\mathrm{int}}(\boldsymbol{x}, \tau - \tau_i)]^4 + [r^L_{\mathrm{int}}(\boldsymbol{x}, \tau_i - \tau)]^4} \tag{3}$$

It is worth noting that such a weighting also improves the robustness of the interpolation with respect to metrology defects localized in space because they are likely to result in low values of the Lagrangian correlation coefficient.

The time evolution of the autocorrelation coefficient interpolated from the few discrete values known from dual-PIV measurements to an arbitrary high time resolution can then be Fourier transformed to obtain a spectral estimator of the power density of velocity. For a convection-dominated flow, such a spectral estimate should be accurate up to the equivalent Nyquist frequency obtained by dividing the convection velocity by twice the grid resolution along the direction of convection.

## III. Experimental and Numerical Setup

### A. Experiments

In principle, dual-PIV systems consist of two independent PIV systems observing the same field of view. Unlike classical time-resolved PIV systems featuring temporal resolutions of up to about 50 kHz [5,6] with a poor spatial resolution, dual-PIV systems allow 1) the determination of certain temporal information also in a high-speed flow (see for example [7–16]), where frequencies of about 100 kHz are required to resolve the turbulent microscales, and give insight into the temporal development of the flow, while 2) maintaining the same high spatial resolution as in classical PIV systems.

The key technology of our dual-PIV system [2], designed in collaboration with DantecDynamics, is frequency-based image separation: two lasers of different wavelengths illuminate the field of view. Image separation is achieved with color filters placed in front of the cameras.

**Table 1 Flow parameters**

| $M_\infty$ | $p_0$ | $T_0$ | $U_\infty$ | $\delta_{99}$ | $Re_\theta$ | $\alpha$ | $L$ |
|---|---|---|---|---|---|---|---|
| 2.0 | 40,500 Pa | 295 K | $510\ \mathrm{m\cdot s^{-1}}$ | 11 mm | 4850 | 8.5 deg | 58 mm |

The present work uses a dual-PIV setup that has been widely described and characterized in Schreyer et al. [2], to which the reader can refer for further information.

This system is used to measure the velocity correlations for a $M = 2$ shock reflection whose flow parameters are given in Table 1. Measurements consist of the sampling of 2000 dual image pairs for each of the 17 time delays listed in Table 2. The selection of the shortest time delays is similar to the one used in [3] to reconstruct velocity spectra from boundary-layer measurements up to 150 kHz using the method described in the first part of Sec. II. The larger time delays yield a lower frequency bound of 1 kHz. The theoretical bandwidth of the reconstructed spectra should therefore include both the $St_L = fL/U_\infty \simeq 0.3$ to 0.5 frequency band associated with the mixing layer and shedding structures [1] and the $St_L > 1$ frequency band related to the turbulence.

Acquired PIV recordings are analyzed using Dynamic Studio V4.0 from Dantec Dynamics. The PIV images are first cropped ($4008 \times 752\ \mathrm{pixel}^2$), leading to a field of view of $113.5 \times 21.3\ \mathrm{mm}^2$ and a spatial resolution of 35.3 pixel/mm. Then, the minimum pixel value is calculated and subtracted from the original picture to minimize noise and laser reflection at the wall. Cross-correlation is made iteratively, using deforming windows, from an interrogation area of $72 \times 36\ \mathrm{pixel}^2$ to a final cell size of $32 \times 16\ \mathrm{pixel}^2$, with an overlap between cells of 50%. Finally, a range validation is applied as well as a $N\sigma$ validation ($N = 6$). Only the validated velocity vectors are used for statistics and interpretation. In this configuration, the final number of vectors per field is $247 \times 94$.

### B. Large-Eddy Simulations

The flow under study is fully turbulent with a moderate Reynolds number and develops low-frequency unsteadiness. A turbulence modeling relying on the large-eddy simulation method appears therefore to be a good candidate to perform time-accurate computations. As a matter of fact, LES has been proved to be a suitable modeling to resolve reflecting shock/turbulent boundary-layer interactions of the type described previously. The LES modeling resulted in accurate predictions of the mean features of the flow [17] and of the low-frequency unsteadiness, in good agreement with experiments [18,19].

The various computations are performed using ONERA's FLU3M solver that has been extensively used in the recent years to successfully analyze compressible flows either by LES or DNS [20,21]. The numerical scheme is designed to be able to capture the shock while meeting the LES requirement of very low dissipation in the turbulent region [22]. This is achieved by adding the dissipative part of the Roe scheme [23], modulated by Ducros's sensor [24], to a second-order centered scheme. The subgrid filtering is implicitly provided by the mesh, and the subgrid modeling relies on the selective mixed-scale subgrid model, well suited for compressible wall bounded flows [25]. Time integration is achieved by means of a second-order accurate implicit Gear scheme [26]. The time step listed in Table 3 leads to maximum Courant-Friedrichs-Levy number of about 11, making the implicit time filtering negligible with respect to the implicit grid filtering. The resulting nonlinear system is solved iteratively at every time step with seven subiterations, yielding a reduction of the residuals of about two orders of magnitude.

Following [17], the computations aim at reproducing only the midspan part of the wind tunnel, excluding the influence of the side walls. Periodic boundary conditions are consequently used in the spanwise direction. The inflow and outflow boundaries of the domain are located $10\delta$ away of the interaction region and rely on a characteristic boundary condition. The fully turbulent inflow boundary condition is obtained by means of a variant of the synthetic eddy method that was demonstrated [18] to be able to recover adequate first- and second-order statistics of an $M = 2.3$ boundary

**Table 2 Set of time delays available from the dual-PIV measurements**

| No. | 1 | 2 | 3 | 4 | 5 | 6 | 7 | 8 | 9 | 10 | 11 | 12 | 13 | 14 | 15 | 16 | 17 |
|---|---|---|---|---|---|---|---|---|---|---|---|---|---|---|---|---|---|
| $\tau_i$, $\mu$s | 5 | 10 | 20 | 40 | 60 | 80 | 100 | 140 | 180 | 220 | 260 | 300 | 340 | 380 | 420 | 460 | 500 |

**Table 3 Simulation parameters**

| Label | Cell count | Domain span | $\Delta x^+$ | $y_0^+$ | $\Delta z^+$ | Time step, s | Duration, s |
|---|---|---|---|---|---|---|---|
| $S$ | $34 \times 10^6$ | $3\delta_{99}$ | 28 | 0.85 | 11 | $1.75 \times 10^{-7}$ | 1.2 |
| $E$ | $68 \times 10^6$ | $6\delta_{99}$ | 28 | 0.85 | 11 | $1.75 \times 10^{-7}$ | $4 \times 10^{-2}$ |
| $F$ | $74 \times 10^6$ | $3\delta_{99}$ | 19 | 0.75 | 8.8 | $1.50 \times 10^{-7}$ | $7.2 \times 10^{-2}$ |

layer within a distance from the inflow lower than $10\delta_{99}$. The main parameters of the methods are set using data from the LES of an $M_\infty = 2$ boundary layer [3].

Three meshes, respectively labeled $S$, $E$, and $F$ in Table 3, have been designed to match the resolution required to solve wall-bounded flows by LES. The $E$ mesh is derived from the standard $S$ mesh by doubling both the span and the number of cells in the spanwise direction. It is used to assess the absence of lateral confinement. The fine $F$ mesh is obtained by increasing the cell count by 40, 30, and 20% in the streamwise, spanwise, and wall-normal directions, respectively.

The $E$ and $F$ computations were designed mainly for validation purposes; the simulated physical time is thus limited to 0.04 and 0.072 s, respectively. These values correspond to about 10 and 18 periods of the low-frequency unsteadiness of the flow, therefore making it possible to achieve acceptable statistical convergence even if spectral quantities are considered. The $S$ simulation aims at obtaining far more converged data to reliably analyze the low-frequency unsteadiness developing in the separated region. Consequently, the simulated duration is set 30 times larger than the one retained for the $E$ computation, resulting in statistics computed over more than 300 low-frequency periods. This value is at least 2 to 10 times higher than the ones found in the literature [18,19,22,27,28]. Velocity, density, and pressure data over various horizontal, vertical, and transverse planes are stored on disk with a 285 kHz sampling rate, high enough for preserving the frequency band below 100 kHz from significant aliasing.

### C. Validation

The $S$, $E$, and $F$ result in a similar development of the interaction, as seen from the dividing streamline (solid), sonic line (dashed), and the shock location (dotted) plotted in Fig. 2a. Moreover, theses computations yield the same interaction length of $57 \times 10^{-3}$ m as the experiments, whereas LES [18,19,27], matching the flow parameters of previous $M = 2.3$ shock–reflection experiments carried out in IUSTI's wind tunnel, resulted in an underprediction of the interaction length. Such an underestimation can be traced back to a spanwise inhomogeneity of the flow induced by confinement through the side walls [22,29,30] that was not taken into account in the aforementioned LESs, which are based on periodic side boundary conditions. The present $M = 2$ experimental setup results in a lower side confinement than the previous $M = 2.3$ setup due to a lowering of the shock generator by 15 mm, resulting in a decrease of the height-to-width ratio, which is known to be a reliable predictor of the confinement level [30]. The milder spanwise inhomogeneity of the new experiments is demonstrated by the fact that the present LESs are able to predict accurately the length of the interaction region despite the use of periodic side boundary conditions.

This agreement on the streamwise length scale allows the direct comparison of LES and PIV velocity data, without any rescaling. The evolutions along the interaction region of the mean streamwise velocity $\langle u \rangle$, of the streamwise velocity variance $\langle u'^2 \rangle$, and of the cross-Reynolds stress $\langle u'v' \rangle$ are plotted in Figs. 2b–2d, respectively. It is first seen from these figures that the three computations yield profiles that collapse almost perfectly. The comparison between mean velocity profiles obtained from experiments and LES further shows that the computations accurately reproduce the streamwise development of the interaction. The two most noticeable discrepancies for the $\langle u \rangle$ profile are found at the feet of the incident shock/expansion fan ($x = 0.31$ m for $y > 5 \times 10^{-3}$ m) and in the relaxation region downstream of the reattachment point ($x > 0.33$ m). The reason behind the first discrepancy is unclear, but the second one could be an indication that the experiments are still subject to a mild spanwise confinement. Wang et al. [30] show that the interaction of the incident shock with the side boundary layers (occurring when side walls are taken into account in the computation) induces on the midplane a stepped lowering of the flow downstream of the apex of the separated region as compared to the corresponding spanwise homogeneous computation. Indeed, such a difference is found also in the current study when comparing the streamlines computed from the experimental and computational flowfields, drawn on Figs. 3a and 3b, respectively.

Another difference between computations and experiments is related to the mixing layer developing above the first half of the separated region. The two-dimensional turbulent kinetic energy

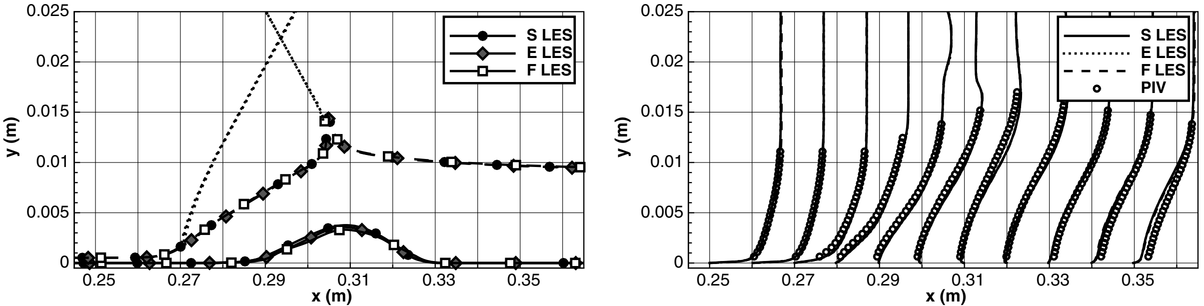

**a) Flow organization** **b) $\langle u \rangle$**

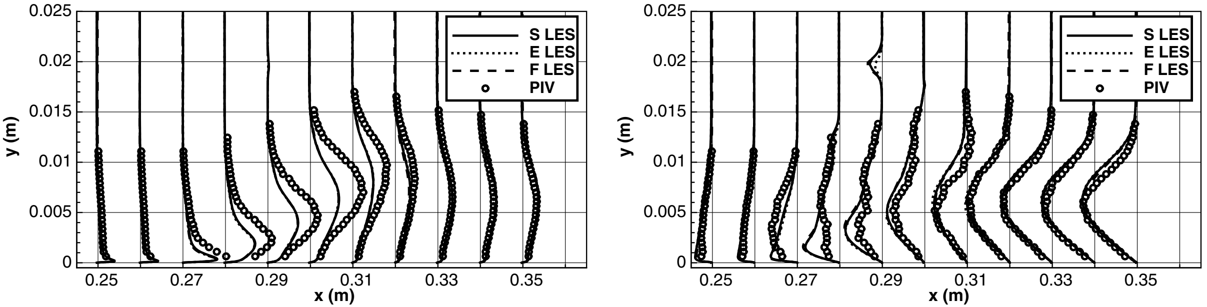

**c) $\langle u'^2 \rangle$** **d) $\langle u'v' \rangle$**

**Fig. 2 Comparisons between the three LES and the PIV measurements.**

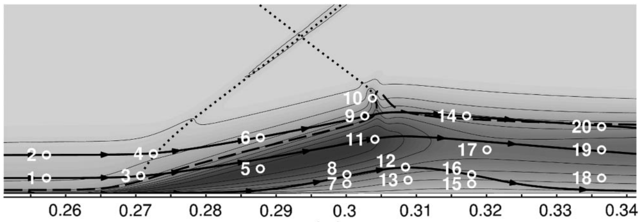

**a) Large-eddy simulation**

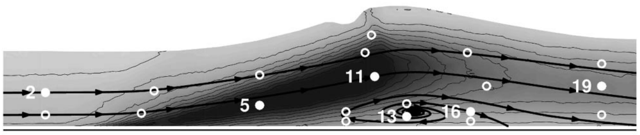

**b) Experiments**

**Fig. 3 Locations of the velocity probes, superimposed on streamlines and isocontours of $k_{2D}$.**

$k_{2D} = 1/2(\langle u'^2\rangle + \langle v'^2\rangle)$ maps plotted in Fig. 3 show that the mixing layer undergoes a rather similar organization in space for the experiments and the computations. The energy content of the mixing layer is, however, significantly higher for the experiments than for the computation, as seen from the contour levels (associated to the same values for both maps). LES underestimates the kinetic energy level by about 35% mainly because of the 40% underestimation of $\langle u'^2\rangle$, as quantified from the profiles in Fig. 2c. This figure also shows a slight upward shift of the location of the maxima for the experiments.

Surprisingly, no similar increase and shift are found when considering $\langle v'^2\rangle$ (not shown for the sake of conciseness) and $\langle u'v'\rangle$ shown in Fig. 2d. Moreover, differences between profiles of the streamwise velocity fluctuation vanish in the shedding region downstream of the bubble's apex. These are indications that the higher values for $\langle u'^2\rangle$ found in the experiments may not be fully related to vortical, Kelvin–Helmholtz-like structures developing within the mixing layer and being shed downstream from the apex of the separation bubble. The spectra of the streamwise velocity computed from the dual-PIV data will help clarify this point (see Sec. V).

The reliability of the reconstruction method required to make the computation of these spectra feasible will be evaluated a posteriori using the highly converged $S$ LES database. It is consequently of importance to ensure that the grid convergence achieved for statistical data extends to spectral measurements to draw trustworthy information from the validation process addressed in Sec. IV.A. Twenty locations distributed over all of the various regions of a shock/boundary-layer interaction have been selected for the evaluation. They are plotted in Fig. 3a and correspond to 1) the incoming boundary layer: probes 1 and 2; 2) the mixing layer developing over the separated region: probes 5 and 11; 3) the edge of the potential region: probes 6, 9, 14, and 20; 4) the inner part of the separated region: probes 7, 13, and 15; 5) the edge of the separated region: probes 8, 12, and 16; and 6) the relaxation region: probes 17, 18, and 19.

Three extra probes located in regions of high intermittency, induced by the motion either of the head shock (3 and 4) or the reflection of the incident shock (10), are also considered. It is worth recalling that no rescaling is used when comparing experimental and numerical data. Consequently, the locations of the experimental probes, displayed in Fig. 3b, exactly match the locations of the LES probes.

For the sake of conciseness, only six locations among 20 have been retained to compare the spectra obtained from the various LES and from the dual-PIV experiments. They are highlighted in Fig. 3b. This selection encompasses all the important regions of the interaction and results in spectra with significantly distinct features. It thus makes the comparison/validation easier. The power spectral densities (PSD) of the streamwise velocity computed using the unsteady data sampled from the three LES at those six locations are plotted in Fig. 4. The three computations result in similar spectra because the differences found are insignificant. They result either from differences in the sampling duration (statistical uncertainty of the spectrum's estimates, levels in the low-frequency region) or from differences in the sampling rate (aliasing in the high-frequency region). It demonstrates that grid convergence is achieved for the $S$ computation even for spectral measurements.

## IV. Evaluation of the Reconstruction Methods

### A. A Posteriori Assessment Using the Large-Eddy Simulation Database

The $S$ LES database described in the previous section is used to test the ability of the cubic natural spline (i.e., with null second derivatives as boundary conditions for $\tau = -\tau_n$ and $\tau = \tau_n$) interpolation and of the interpolations based on the cross-correlation to provide reliable spectral estimates. The auto/cross-correlation data required to estimate the spectrum have been computed up to a time delay 1.3 larger than the typical time scale associated with the low-frequency unsteadiness found in the shock/boundary-layer interaction flow consideration. These data are highly converged because they are built from a time averaging over a duration of about 300 periods of the low-frequency unsteadiness. The statistical convergence is further reinforced by averaging the correlations over 14 spanwise-distributed, mostly uncorrelated planes. The resulting correlations and exact spectra consequently exhibit very low levels of statistical uncertainty. It is also worth noting that the spatial resolutions of the dual-PIV measurements and the $S$ LES data are close to each other. Also, the experimental and LES mean velocity fields are in good agreement, as seen in Sec. III.C. Consequently, dual-PIV and LES-based spectral reconstructions based on cross-correlation through Taylor's hypothesis should theoretically be restricted to almost similar upper frequency limits based on the equivalent Nyquist frequency mentioned in Sec. II.

Autocorrelation reconstructions and the derived spectra have been computed for two distinct sets $\Theta^{\mathrm{LES}}$ of time delays encompassing 13 and 17 discrete time delays, respectively, as listed in Table 4. The set $\Theta_2^{\mathrm{LES}}$ matches the experimental set described in Table 2 as close as possible, given an LES sampling rate of approximately 285.7 kHz. The set $\Theta_1^{\mathrm{LES}}$ is based on an almost uniform sampling of the cross-correlation functions that was demonstrated to be sufficient to achieve accurate estimates of velocity spectra for a supersonic boundary layer using the original method of Schreyer et al. [3].

The rms of the interpolation error, defined as the weighted difference between the autocorrelation coefficient computed from the LES data at the full sampling rate and the autocorrelation coefficient reconstructed by interpolating from subsets $\Theta_k^{\mathrm{LES}}$, is plotted in Fig. 5 for the 20 selected probes. The weighting at delay time $\tau_i$ is chosen equal to the inverse of $\tau_i$ to give preeminence to the low time delay errors that are associated with errors in the high-frequency region of the derived spectra. The resulting metric faithfully reflects the accuracy of the spectrum estimates in a synthetic way.

The interpolations based on cross-correlation, either in its original or refined formulation, generally outperform the cubic-spline interpolation as far as set $\Theta_1^{\mathrm{LES}}$ is considered (see Fig. 5a). Notable exceptions are found for probe 10 on the one hand and probes 7, 8, 12, 13, 15, 16, and 18 on the other hand. The high error level for probe 10 arises from its location in a highly intermittent region, which makes a significant part of the total power unrelated to any convective process. Consequently, convection-driven interpolations cannot be expected to perform very well in such regions. The seven other error-prone probes are associated with large integral time scales. The coarse discretization of set $\Theta_1^{\mathrm{LES}}$ is thus less penalizing for the cubic-spline interpolation for these probes than for the other locations exhibiting shorter time scales.

Almost no differences between the original and refined interpolation methods are found in Fig. 5a. It is worth noting that, because of the rather coarse discretization of the time delays at low $\tau$ associated with set $\Theta_1^{\mathrm{LES}}$, only cross-correlations at time delays $\tau_i = \pm 21\ \mu\mathrm{s}$ and $\tau_i = \pm 63\ \mu\mathrm{s}$ are taken into account when computing the displacement path of the convected frame of reference. As a consequence, the displacement estimates obtained from the smoothed piecewise linear approximation boil down to a straight displacement resulting from the simple linear approximation, as seen for the mixing layer region in Fig. 1a. It thus makes the original and refined methods differ by the

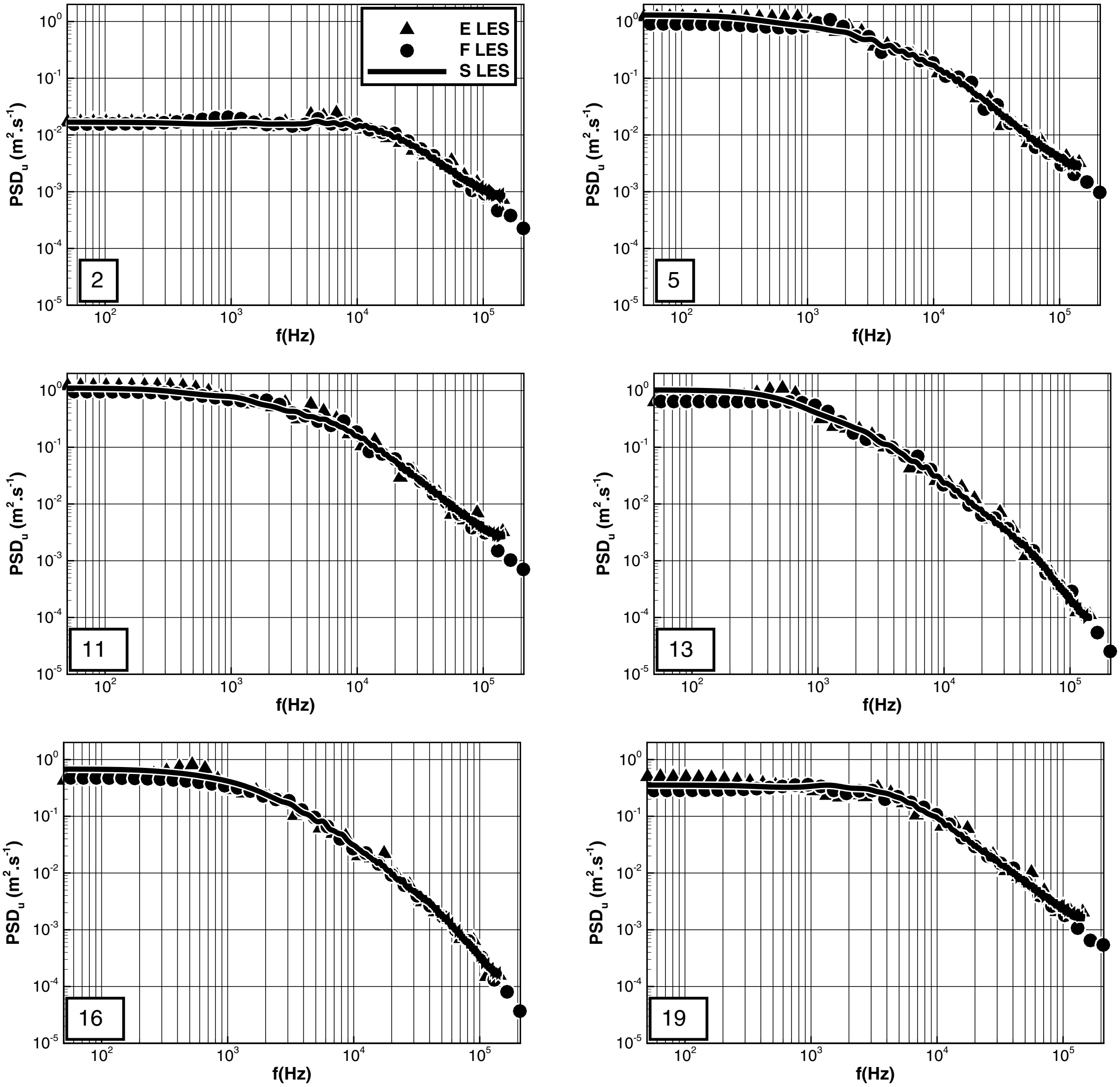

**Fig. 4 Streamwise velocity spectra computed from LES data for the locations identified in Fig. 3b.**

Lagrangian correlation-based weighting of Eq. (3) only. This weighting consequently seems to have a modest impact on the improvement of the accuracy. Main differences are found for probes 1 to 4. For the two latter ones, upstream interpolations are favored over downstream ones because correlation levels are decreasing downstream of the head shock. In contrast, the downstream interpolations are favored for probes 1 and 2 because these sensors are located close to the upstream bound of the sampling domain, making the estimation of the upstream displacement rather unreliable. This illustrates the adaptivity of the space weighting defined in Eq. (3) within regions exhibiting a loss of accuracy that alters the prediction of the convected frame of reference. Such mispredictions are more likely to occur in PIV measurements than in numerical simulation data because of seeding difficulties, among others.

When moving from set $\Theta_1^{\mathrm{LES}}$ to set $\Theta_2^{\mathrm{LES}}$, the plots of Fig. 5b show that the interpolation error is significantly reduced for all schemes and all locations, with the unsurprising exception of probes 3, 4, 9, and 10 for the cross-correlation-based interpolations. As already mentioned, these probes are located in a region of high intermittency, making the convection assumption on which interpolation schemes from cross-correlation are built mostly irrelevant. Apart from these probes, the cubic-spline interpolation appears to be on a par with convection-based interpolations within the interaction region, whereas it is outperformed upstream and downstream of that region (probes 1, 2, 19, and 20). Note that the competitive advantage of the cubic spline found in regions of large integral time scale for set $\Theta_1^{\mathrm{LES}}$ no longer exists for set $\Theta_2^{\mathrm{LES}}$ because of the refined discretization at low time delays.

No clear evidence of an improved accuracy associated with the use of the refined interpolation scheme over the original one is found in Fig. 5b. It is, however, worth mentioning that the present, refined scheme yields results that are less sensitive to the choice of the threshold on the Lagrangian autocorrelation used when seeking for the location of the convected frame of reference than the ones obtained

**Table 4 Sets of time delays used to interpolate the autocorrelation functions**

| $\tau_i$, $\mu$s | 3.5 | 10.5 | 21 | 42 | 63 | 84 | 105 | 147 | 189 | 231 | 273 | 315 | 357 | 399 | 441 | 483 | 525 |
|---|---|---|---|---|---|---|---|---|---|---|---|---|---|---|---|---|---|
| $\Theta_1^{\mathrm{LES}}$ (13) | — — | — — | × | — — | × | — — | × | × | × | × | × | × | × | × | × | × | × |
| $\Theta_2^{\mathrm{LES}}$ (17) | × | × | × | × | × | × | × | × | × | × | × | × | × | × | × | × | × |

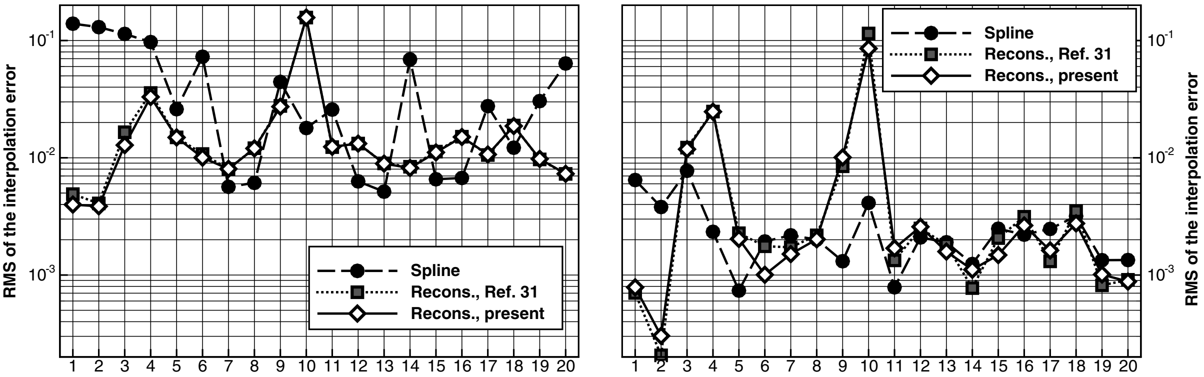

a) $\Theta_1^{LES}$ set

b) $\Theta_2^{LES}$ set

**Fig. 5 Weighted interpolation error for various interpolation schemes at two time sets.**

from the original method of Schreyer et al. [3]. Consequently, the refined method results in a more robust interpolation scheme.

Typical power spectra, either exact or computed from the interpolated autocorrelation functions associated with sets $\Theta_1^{\mathrm{LES}}$ and $\Theta_2^{\mathrm{LES}}$, respectively, are plotted in the two first and two last columns of Fig. 6, respectively. For the sake of clarity, spectra estimates obtained from the original method [3] have not been retained because they are mostly identical to the ones coming from the present refined approach. The plots from the second column of Fig. 6 confirm the information extracted from the interpolation error in Fig. 5a for the cubic-spline interpolation with the coarser time delay set $\Theta_1^{\mathrm{LES}}$. It is visible that spectra relying on this method exhibit more or less severe distortions between medium- and high-frequency regions, mostly for probes associated with high convection velocity such as probes 2, 4, and (to a lesser extent) 5 and 10. This can be traced back to a too-coarse discretization of the cross-correlation in the region where the time delay is lower than the integral time scale, as shown in [3].

Estimates built from the cross-correlation using $\Theta_1^{\mathrm{LES}}$ (first column of the figure) are more accurate, except for the spurious peaks/oscillations found for probes 3 and 4 located in the region of high intermittency associated with motion of the shock system. It has, however, to be noted that the global shape of these spectra is preserved, with the exception of probe 10, where the most severe intermittency occurs. Flaws of lower severity are also found; the spectral densities are overpredicted in the high-frequency band when probes are located within region where the typical convection velocity is as low as $50\ \mathrm{m} \cdot \mathrm{s}^{-1}$. Such a low value, associated with a streamwise grid resolution of $3.6 \times 10^{-4}$ m, yields an equivalent Nyquist frequency $f_{\mathrm{Nyquist}}^{\mathrm{conv}} \simeq 70$ kHz. Aliasing consequently occurs for the frequency band bounded by $f_{\mathrm{Nyquist}}^{\mathrm{conv}}$ and the Nyquist frequency of the exact spectrum, equal to 145 kHz, as seen for probe 15 in Fig. 6, and similarly found for probes 7, 8, 12, 13, and 16.

Refining the time discretization in the low-time-delay region leads to a reduction of the aliasing at these locations, enlarging the frequency band over which the spectra obtained the reconstruction based on the cross-correlation and the exact ones match each other by about 30 kHz, as evidenced for probe 15 from the lower plot of the third column of Fig. 6. Estimates obtained from cubic-spline interpolation in the low convection velocity regions also take advantage of the refined discretization, but to a lesser extent, resulting in a matching frequency band that is typically narrower by 20 kHz when compared to the one achieved from a convection-based interpolation, as seen in the lower right plot of Fig. 6. In the other regions of the flow, both the spline-based and cross-correlation-based spectra interpolated from the $\Theta_2^{\mathrm{LES}}$ set exhibit an almost perfect agreement with the exact spectra. Exceptions are only found, once again, in strongly intermittent regions, as for probes 4 and 5, where the reconstruction from cross-correlation perform averagely.

Eventually, the interpolation based on the use of the cross-correlations appears to be a safer choice for estimating power spectra. It behaves more consistently than the cubic-spline interpolation when the time delay set, from which the interpolation are computed, varies. The refinement of the original interpolation method [3], specifically introduced to deal with highly inhomogeneous regions of the flow, only marginally improves the accuracy of the interpolation, but the robustness of the method is significantly increased. Last, it is rather easy to identify, from educated guess, the locations where the interpolation scheme could perform poorly, namely the regions that are not convection-dominated and the region of low convection velocity where aliasing can occur. In those regions, the cubic-spline interpolation is an interesting alternative, but it must be a posteriori ensured from the cross-correlation functions that the time delay discretization is fine enough to prevent distortions of the spectra that are not easily detected otherwise.

### B. A Priori Accuracy Metrics

Even though regions where the interpolation scheme based on cross-correlation is unlikely to be accurate can generally be identified a priori from basic knowledge of the flow physics, it is desirable to define objective metrics allowing intrinsic analyses of the accuracy of the reconstructed spectra.

At first, there is a need for a metric that helps identify regions where the convection hypothesis is disproved because the convection hypothesis is the most crucial element of the interpolation scheme. Taylor-like hypotheses can be invalidated for several reasons; among others are a local predominance of nonconvective physics, a convection dominated by motion normal to the measurement plane, and a dispersive convection, for which the convection velocity varies with scales. Moreover, even if valid, the convection hypothesis can be invoked over limited distance/duration only. Last, spectral reconstruction based on a convection hypothesis is band-limited because of the finite spatial resolution of the data; a criterion allowing to define an equivalent Nyquist frequency has already be given at the end of Sec. II.

Taylor's frozen turbulence hypothesis mathematically translates into the requirement of a Lagrangian autocorrelation coefficient being close to unity for the lag time/separation distance under consideration. It is worth noting that, under this assumption, fluctuations in time can be reconstructed from fluctuations in space by invoking convection even for inhomogeneous flows by simply scaling the fluctuations according to the ratio of the local standard deviation. The Lagrangian autocorrelation coefficients are most generally not known directly but can be estimated by seeking for each lag time the maximum value of the cross-correlation coefficient, as mentioned in Sec. II.

If the flow is locally nondominated by convection, locations of the maximum of the cross-correlation coefficient will not be distributed along a regular path, and the estimated Lagrangian autocorrelation coefficients will generally not display a smooth decrease with time. Probe 10 is located in a flow region dominated by a nonconvective intermittency, and the estimated Lagrangian autocorrelation coefficient indeed varies in a nonmonotonic way, as seen in Fig. 7a.

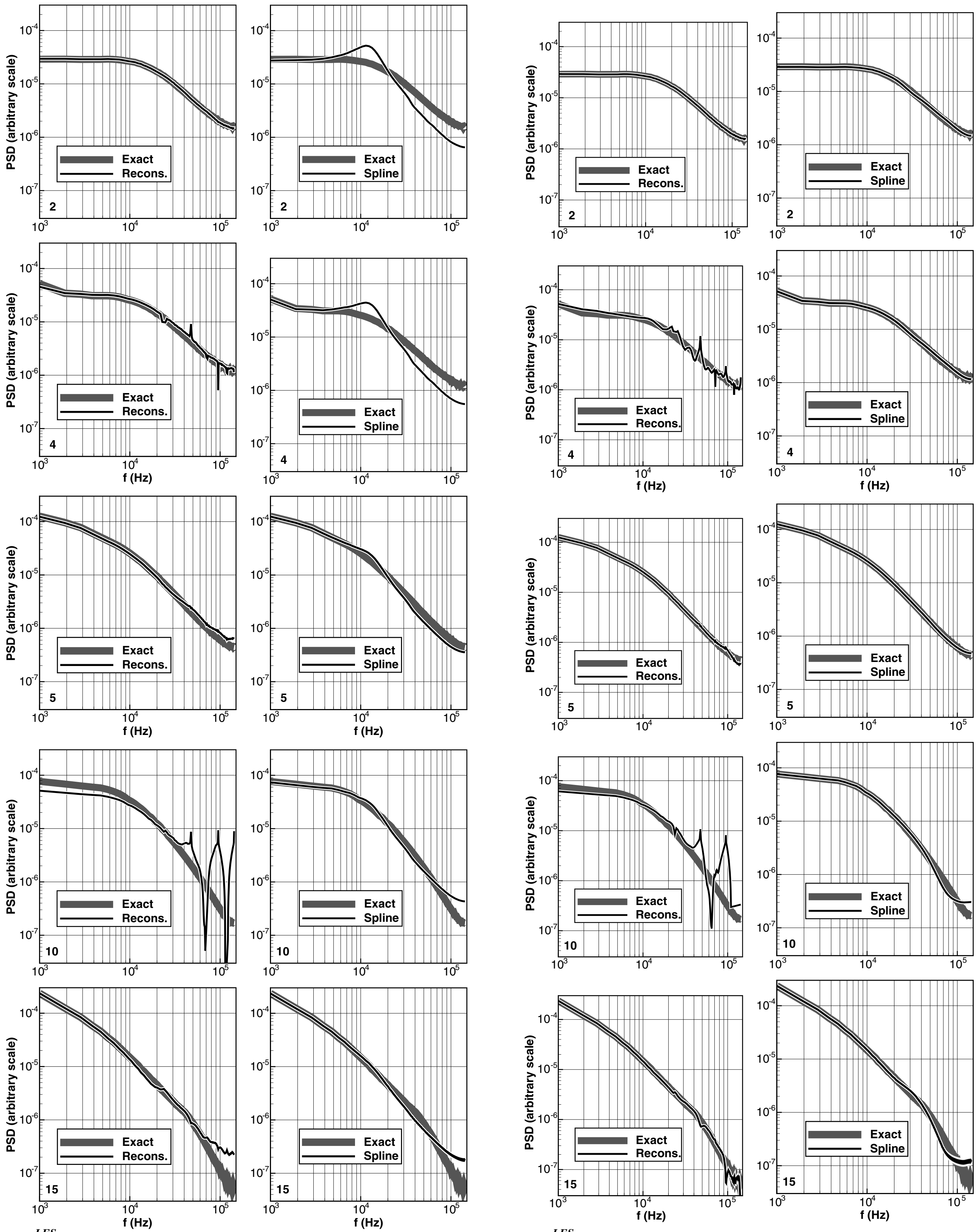

**a)** $\Theta_1^{LES}$ **set**

**b)** $\Theta_2^{LES}$ **set**

**Fig. 6 Exact and reconstructed normalized spectra of the streamwise velocity at five selected locations.**

This is due to the fact that maxima of the cross-correlation coefficient are found at the same location $\xi = 0$ for the lag time interval $[-10, 7.5\ \mu s]$, denoting a lack of convection for the energetically prevalent physics.

When the flow physics is indeed convective, values of the estimated Lagrangian autocorrelation coefficient are direct indicators of the validity of the frozen turbulence hypothesis with in-plane motion. For instance, if the convection occurs mostly in the direction

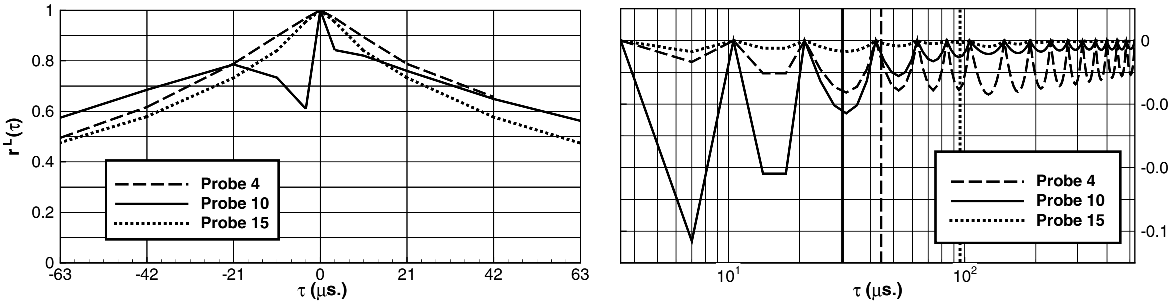

**a) Estimated lagrangian autocorrelation coefficient** **b) Estimated interpolation error**

**Fig. 7 Accuracy metrics. The vertical lines on the left plots denote the integral time scale.**

normal to the measurement plane, the estimated Lagrangian autocorrelation will drop sharply down to values close to zero. Note that this cannot occur in the present LES data set because the flow is strictly homogeneous in the spanwise direction due to spanwise periodicity; as a consequence, the mean convection motion remains in-plane as well as the maxima of the cross-correlation at any given lag time. Moreover, experiments [31] as well as computations including side walls [22,29,30] have demonstrated that such shock/boundary-layer interactions are quasi-homogeneous in the spanwise direction over a central region encompassing about 10 to 20% of the total width of the wind tunnel.

If a dispersive convection is considered, the motion obtained from the maxima of the cross-correlation coefficient is an energetically weighted mean of the motions associated with the various scales. Consequently, it has to be associated with energetically prevailing structures. For free shear flows being energetically dominated by large, quasi-deterministic, vortical structures coming from flow instabilities that induce very high levels of velocity fluctuation, it is well known that small-scale fluctuations in time are not well predicted by the frozen turbulence hypothesis based on such a weighted, global convection velocity. This is mostly due to the fact that the convection velocity associated with these scales of low energy somewhat differs from the global convection velocity. As a consequence, the location at which the small-scale information has to be sought to recover the temporal variation is all the more incorrectly predicted because large time delays are considered. It is worth noting that such an error is difficult to detect from the values of the estimated Lagrangian autocorrelation because the contribution associated with small scales is weak because they carry little energy.

It must, however, be emphasized that, in the context of the present interpolation method, this drawback is strongly mitigated because the convection hypothesis is invoked for a very short duration corresponding to the maximum value of the difference between two consecutive sampled time delays $\tau_i$ and $\tau_{i+1}$. Moreover, half of the $\tau_{i+1} - \tau_i$ difference is a better estimate of the typical duration over which convection is assumed because the interpolation scheme for $\tau_i \le \tau \le \tau_{i+1}$ is based on a time weighting of estimates invoking upstream convection from $\tau_i$ and downstream convection from $\tau_{i+1}$. As a consequence, locations at which the information for the large and small scales can be optimally recovered differ only by little.

In the present setup, half of the maximum difference between two sampled time lags is 21 $\mu$s. A difference of 10% of $U_\infty$ between two convection velocities will therefore translates into a difference of displacement of about 1 mm, a value that corresponds to 10% of the boundary-layer thickness, to less than 2% of the interaction length, and to about twice the lengths of both the PIV and LES cells. Moreover, small scales are generally associated with high frequencies, whose accurate prediction of the spectral content is mostly linked with the accurate prediction of the autocorrelation coefficient for low time delays. In that region, differences between two consecutive sampled lag times are further reduced by a factor of 2 (set $\Theta_1^{\mathrm{LES}}$) and 4 to 12 (set $\Theta_2^{\mathrm{LES}}$), making the error associated with dispersive convection negligible.

As a consequence, dispersion errors related to a multiscale convection cannot account for the spectral discrepancies seen in Fig. 6 for probes 4 and, to a lesser extent, 15. Moreover, it is seen in Fig. 7a that the values of the estimated Lagrangian autocorrelation are higher than 0.7 up to the typical duration of $\tau = 21$ $\mu$s. over which the convection assumption is invoked. Another metric should therefore be defined to explain these discrepancies.

A careful examination of differences between the exact and reconstructed autocorrelation coefficients obtained for these two probes shows that the reconstruction error is due to a superposition of 1) a convective process whose associated autocorrelation coefficient progressively tends toward zero, and 2) a nonconvective process (or process with very low convection velocity such as the bubble breathing) of low, almost-constant, autocorrelation coefficient.

It implies that the convective process is dominant at low to medium lag times, whereas it is negligible at larger time delays. In that region of large time delays, the interpolation scheme based on the convection assumption therefore results in improper predictions rapidly tending toward zero. However, the scheme is used only to reconstruct the autocorrelation coefficient between two sampled values. The interpolation error in the large lag time region due to the occurrence of a nonconvective process with a large integral time scale therefore oscillates between zero for $\tau = \tau_i$ and $\tau = \tau_{i+1}$ and a value roughly equal to minus the constant, nonconvective value for $\tau \simeq 1/2(\tau_i + \tau_{i+1})$.

In the present work, the cross-correlation is sampled with a constant interval between lag times for the large time delays, making the interpolation error almost periodical with a period equal to the lag time sampling interval. When the autocorrelation coefficient is Fourier transformed to obtain the power spectrum, such a quasi-periodic interpolation error translates into spectral distortions in frequency bands centered on integer multiples of the inverse of the sampling period. It therefore explains the oscillations near 24 kHz and its harmonics for probes 4, 10, and 15. It demonstrates that these kinds of spectral distortions, remaining unpredictable based on the sole estimated Lagrangian autocorrelation coefficient, can be anticipated by looking directly at the interpolation error.

In the absence of reference data for the autocorrelation coefficient such as the one provided by the LES data set, the interpolation error obviously cannot be exactly calculated. It can nonetheless be estimated by considering for the reconstruction interval $[\tau_i, \tau_{i+1}]$ the difference between the value of the autocorrelation coefficient sampled for $\tau_i$ (respectively $\tau_{i+1}$) and the value estimated in a backward way (respectively forward way) from the cross-correlation coefficient at $\tau_{i+1}$ (respectively $\tau_i$) using Taylor's hypothesis. These forward and backward estimates can be further refined by averaging estimates obtained by considering positive and negative lag times through the weight function defined in Eq. (3). It is then assumed that the forward error grows linearly from 0 at $\tau = \tau_i$ up to the forward estimate $\epsilon_{\mathrm{est}}^F$ at $\tau_{i+1}$, whereas the backward error decreases linearly from the backward estimate $\epsilon_{\mathrm{est}}^B$ at $\tau_i$ down to zero at $\tau_{i+1}$. The forward and backward estimates are eventually weighted in time using Eq. (2) to obtain a model for the evolution of the interpolation error over the interval $[\tau_i, \tau_{i+1}]$:

$$\epsilon_{\mathrm{est}} = w^T(1 - w^T)(\epsilon_{\mathrm{est}}^F + \epsilon_{\mathrm{est}}^B) \tag{4}$$

Tests using the LES database tend to indicate that such a model is able to reproduce rather faithfully the evolution of the interpolation error between two sampled lag times, despite a tendency in convection-dominated regions to slightly overpredict maximum levels because forward and backward errors tend to increase slower than linearly. The opposite tendency is found for nonconvective regions. It is seen from Fig. 7b that such a model is indeed able to recover the high-amplitude periodic modulations of the error already mentioned for probe 4 at large time delays that result in the severe harmonic distortions found in the estimated spectrum. It is also seen that periodic modulations are also found for probe 15 but in a much milder way, thus explaining that the harmonic distortions of the corresponding spectrum are very weak.

Another type of spectral distortion can be predicted from the plots of Fig. 7b by noting that the logarithmic scale of the $x$ axis makes the area under the curve correspond to the error weighted by the inverse of the time delay. Such a weighting was used in a previous section as a way to put into evidence spectral errors in the high-frequency region. It was also shown in Schreyer et al. [3] that the high-frequency region of a spectrum was distorted if large interpolation errors occur for $\tau$ lower than the integral time scale. Such a high-frequency distortion induces an opposite distortion in another region of the spectrum, most generally the low-frequency one because the integral of the spectrum is normalized to unity as being computed from the autocorrelation coefficient. The large area under the curve found for probe 10 at lag times lower than the integral time scale therefore enables to predict the severe low-frequency/high-frequency distortions that occur in the corresponding spectrum. Because significant periodic errors are also found for this probe at lag times higher than the integral time scale, the small harmonic distortions evidenced in Fig. 6 can also be anticipated.

Even though such a detailed analysis of the error is not carried out, model 4 can be used to estimate the rms of the weighted error for each of the 20 probes. The rms of the estimated interpolation error for sets $\Theta_1^{\mathrm{LES}}$ and $\Theta_2^{\mathrm{LES}}$ is plotted in Fig. 8a in a way similar to the plots of Figs. 5a and 5b dedicated to the rms of the exact error. The curve of the error estimated for set $\Theta_1^{\mathrm{LES}}$ exhibits a much lower dynamics than its exact counterpart because of the tendency of model 4 to overpredict/underpredict errors in regions with/without convection that is exacerbated by the rather crude temporal sampling for low values of $\tau$. The model is, however, able to correctly predict the evolution of the error levels when moving from sets $\Theta_1^{\mathrm{LES}}$ to $\Theta_2^{\mathrm{LES}}$; the error level is greatly reduced in convection-dominated regions and only slightly reduced in other regions. Last, when considering set $\Theta_2^{\mathrm{LES}}$, the estimated error is found to predict rather faithfully the exact error for all the probes.

Taking into account information from Figs. 5, 6, and 8, it appears that an estimated rms error level decreasing down to less than $10^{-2}$ when the sampling set is refined in the low lag time region could be a reliable criterion for accessing the global accuracy of the spectrum estimates. Spectral flaws of low importance can then be further detected by the detailed analysis of the evolution of the estimated error with the lag time. The model defined by Eq. (4) consequently appears to be a reliable metric for evaluating the accuracy of the spectral estimates without any other knowledge than the dual-PIV measurements.

Equation (4) is therefore used to estimate a priori the weighted interpolation error achieved when applying the reconstruction method to the dual-PIV measurements. Estimated errors are also computed from the LES database downsampled by a factor of 171 to consider the same number of samples as the experiments, without spanwise averaging. Statistics computed from the experimental and from the downsampled LES database will consequently achieve a similar level of statistical uncertainty, allowing fair comparisons between them.

Note that it was not possible to derive a spectral reconstruction for probe 10 from the dual-PIV data because this probe is located close to the edge of the seeded region, resulting in a number of validated samples too low to obtain converged second-order statistics. Besides that probe, plots of Fig. 8 demonstrate that the estimated accuracy of the spectral reconstruction is similar for the LES and the experiments, with the notable exception of probe 6. A detailed analysis of the evolution of the interpolation error with the lag time shows that the error at low lag time dominates, making the spectrum estimate at probe 6 prone to opposite low-frequency/high-frequency distortions. Noteworthy, the six probes selected in Sec. III.C to perform comparisons between LES and experimental spectra match the previously defined criterion for accurate spectral reconstruction.

## V. Application to Dual Particle Image Velocimetry Data

After successful validation of the interpolation method, as discussed in the previous section, the cross-correlation-based interpolation scheme defined can now be used to estimate the velocity spectra from the dual-PIV measurements at time delays listed in Table 2. Because of the rather low number of samples (2000) associated with each time delay, the statistical convergence of the spectrum estimates is rather low. Therefore, estimates computed from the cell under consideration as well as for the eight cells surrounding it have been averaged to reduce the statistical uncertainty. Physically, this corresponds to an average over a 1 × 1 mm area. Note that the same average has been applied to the LES spectra shown in the present section for the purpose of fair comparison.

The spectra obtained from the dual-PIV measurements and computed from the LES data are plotted in Fig. 9 for the six locations highlighted in Fig. 3b. Note that, contrary to the plots of Fig. 6, the spectra in Fig. 9 are not normalized to unity, thus implying that

$$\int_0^{f_{\mathrm{Nyquist}}} \mathrm{PSD}_u(f)\,\mathrm{d}f \equiv \langle u'^2 \rangle$$

It allows direct comparison of the spectral density levels between experiments and LES.

Overall, changes in shape of the spectra from one probe to the other appear rather similar in the experiments and in the computations. The most notable difference is the significantly higher low-frequency energy content found in the experiments for the incoming boundary layer (probe 2), already identified and discussed in [3], as well as

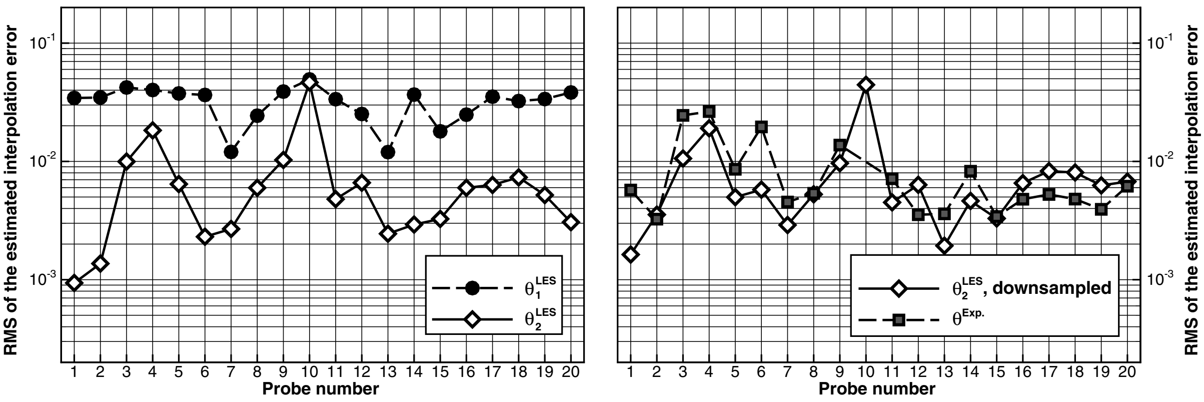

**a) LES** **b) Downsampled LES and experiments**

**Fig. 8 Weighted estimated interpolation error.**

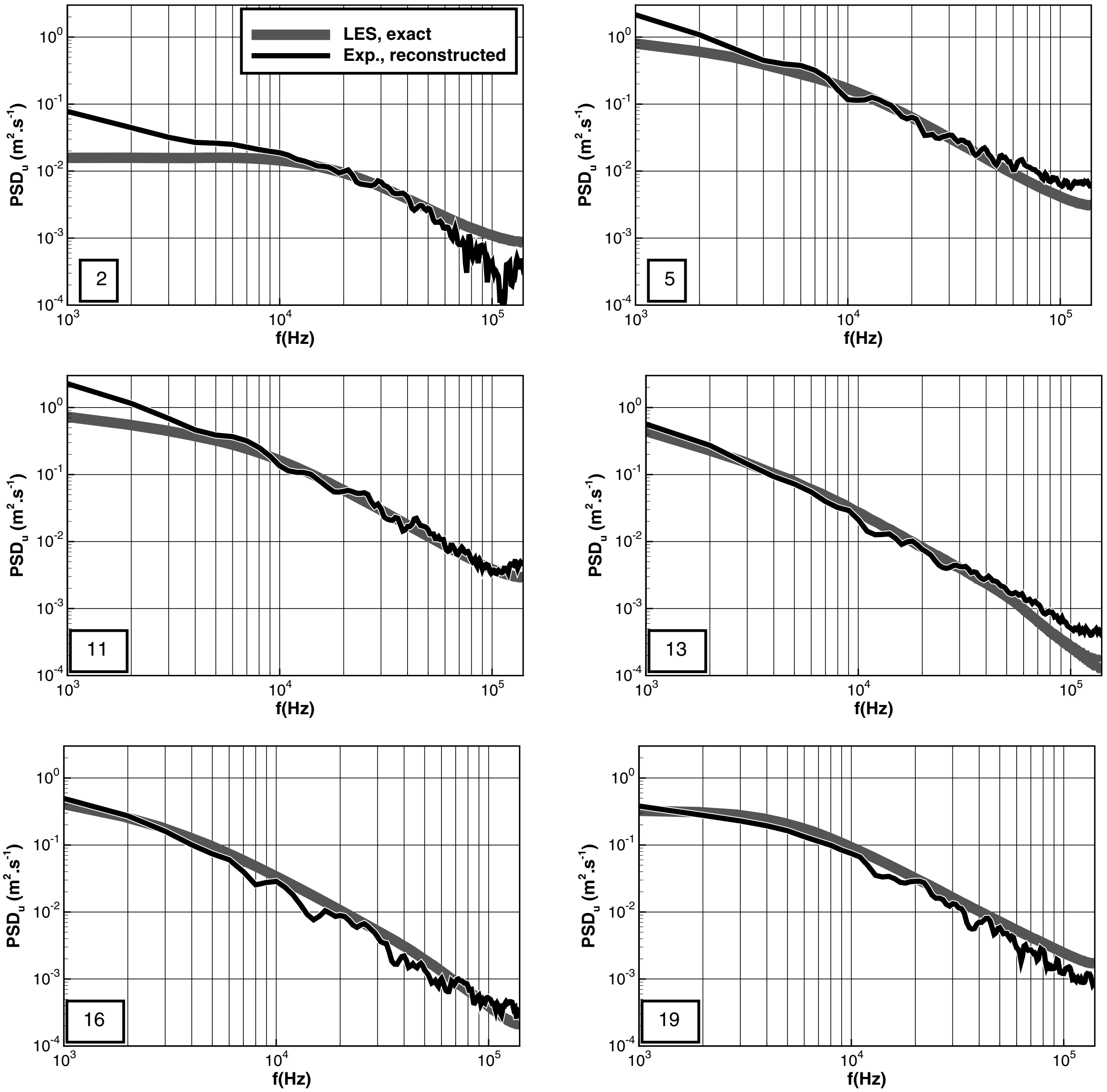

**Fig. 9 Streamwise velocity spectra reconstructed from the dual-PIV measurements with time delays $\Theta^{\mathrm{Exp}}$ and computed from LES data for the locations identified in Fig. 3b.**

inside the mixing layer (probes 5 and 11). Spectra related to probes 5 and 11 demonstrate that the underestimation of the streamwise velocity variance by the LES seen for this probe in Fig. 2c is mainly due to frequencies lower than the frequencies associated with Kelvin–Helmholtz-like structures (4 to 5 kHz for the present interaction, see [1]).

The integration of the spectra of probes 5 and 11 over the frequency range [0, 4 kHz] shows that the amount of variance associated with the low-frequency range in the mixing layer is 60% lower for the LES than for the experiments. As a consequence, the difference in variance between LES and experiments related to this sole frequency band accounts for about 90% of the total variance difference seen in Fig. 2c. The same integration performed for sensor 2, located in the incoming boundary layer, shows that the low-frequency content of the LES is about 70% lower than its experimental counterpart. Note that this latter difference is not induced by an inaccurate turbulent inflow condition because a comparable difference was found in Schreyer et al. [3], whereas the LES of the flat-plate boundary-layer flow studied in that reference was encompassing the whole laminar–turbulent transition process.

Despite this energy deficit in the low-frequency range, the present LES data clearly exhibit low-frequency unsteadiness of both the head shock and the separated bubble but with slightly reduced amplitudes compared to the experiments, as for the previous $M = 2.3$ setup [18]. One consequently may postulate that the low-frequency unsteadiness associated with shock/boundary-layer interactions has indeed a dual origin: 1) induced by the incoming boundary layer [19,32], and 2) inherent in the separated region [33–35].

The origin of the low-frequency energy found in the incoming boundary layer is unclear. Possible explanations include low-amplitude, low-frequency oscillations of the wind-tunnel pressure regulation or the occurrence of the so-called boundary-layer superstructures. However, the Reynolds number based on the momentum thickness of 4850 is a priori too low for such superstructures to develop.

One can remark nonetheless that the experimental boundary layer is developing on the floor of the wind tunnel from an upstream boundary layer that is relaminarized in the divergent section of the nozzle upstream of the test section. Moreover, flow perturbations induced upstream of the nozzle throat have already been found to persist and propagate down to the test section despite the relaminarization [36].

It can also be noted that the experimental low-frequency content of probes 2, 5, and 11 is directly related to large integral time scales and therefore to autocorrelation coefficients that do not tend toward zero for large lag times. These nonzero values are, however, not associated with significant periodic modulations of the interpolation error as the ones found in Sec. IV.B when nonconvective processes with large integral time scale occur. This is a strong indication that the low-frequency content of the boundary layer and mixing layer is convective in nature.

Last, it has also been observed in previous boundary-layer measurements that the $\langle u'^2 \rangle$ profiles were exhibiting a small secondary local maximum near the upper boundary of the logarithmic region (seen for instance in Fig. 2 of Agostini et al. [18]) that could be the signature of such superstructures. Based on these clues, the occurrence of boundary-layer superstructures eventually appears to be a credible candidate for explaining the low-frequency difference between experimental and LES spectra within the incoming boundary layer and the mixing layer. Further studies relying on cross-spectral analysis could help clarify that point.

## VI. Conclusions

A method enabling to compute velocity spectrum estimates through the use of cross-correlation maps obtained from dual-particle image velocimetry (PIV) measurements, already validated for a quasi-homogeneous boundary-layer flow [3], has been extended to deal with strongly inhomogeneous flow such as shock/boundary-layer interactions. The new formulation has been compared to the previous one, demonstrating increased robustness, and has been successfully validated against exact spectra by means of a new, long-time, high-resolution large-eddy simulation (LES) database. Metrics allowing the a priori evaluation of the accuracy of the spectrum estimates have been derived and validated. Spectra computed from dual-PIV measurements have then been compared with LES spectra, demonstrating a good agreement while highlighting differences of possible significant physical consequences.

## Acknowledgments

This work received financial support from the Centre National d’Etudes Spatiales through the research program Aérodynamique des Tuyères et Arrière-Corps as well as from the Labex Mécanique et Complexité. It was granted access to the High Performance Computing resources of Institut du Développement et des Ressources en Informatique Scientifique under the allocation 2014-2a1877 and 2015-2a1877 made by Grand Équipement National de Calcul Intensif for the LES computations. This supports is gratefully acknowledged.

## References

[1] Dupont, P., Haddad, C., and Debiève, J.-F., “Space and Time Organization in a Shock-Induced Separated Boundary Layer,” *Journal of Fluid Mechanics*, Vol. 559, July 2006, pp. 255–277. doi:10.1017/S0022112006000267

[2] Schreyer, A.-M., Lasserre, J. J., and Dupont, P., “Development of a Dual-PIV System for High-Speed Flow Applications,” *Experiments in Fluids*, Vol. 56, No. 10, 2015, pp. 1–12. doi:10.1007/s00348-015-2053-0

[3] Schreyer, A.-M., Larchevêque, L., and Dupont, P., “Method for Spectra Estimation from High-Speed Experimental Data,” *AIAA Journal*, Vol. 54, No. 2, 2016, pp. 557–568. doi:10.2514/1.J054370

[4] Blackman, R. B., and Tukey, J. W., *The Measurement of Power Spectra from the Point of View of Communication Engineering*, Dover, New York, 1958, pp. 11–14.

[5] Beresh, S. J., Kearney, S. P., Wagner, J. L., Guildenbecher, D. R., Henfling, J. F., Spillers, R. W., Pruett, B. O. M., Jiang, N., Slipchenko, M. N., Mance, J., and Roy, S., “Pulse-Burst PIV in a High-Speed Wind Tunnel,” *53rd AIAA Aerospace Science Meeting*, AIAA Paper 2015-1218, Jan. 2015.

[6] Wernet, M., “Temporally Resolved PIV for Space-Time Correlations in Both Cold and Hot Jet Flows,” *Measurement Science and Technology*, Vol. 18, No. 5, 2007, pp. 1387–1403. doi:10.1088/0957-0233/18/5/027

[7] Bridges, J., and Wernet, M., “Measurements of Aeroacoustic Sound Sources in Turbulent Jets,” *9th AIAA/CEAS Aeroacoustics Conference and Exhibit*, AIAA Paper 2003-3130, May 2003.

[8] Bridges, J., “Effect of Heat on Space-Time Correlations in Jets,” *12th AIAA/CEAS Aeroacoustics Conference*, AIAA Paper 2006-2534, May 2006.

[9] Fleury, V., Bailly, C., Jondeau, E., Michard, M., and Juve, D., “Space-Time Correlations in Two Subsonic Jets Using Dual Particle Image Velocimetry Measurements,” *AIAA Journal*, Vol. 46, No. 10, 2008, pp. 2498–2509. doi:10.2514/1.35561

[10] Ganapathisubramani, B., Longmire, E. K., Marusic, I., and Pothos, S., “Dual-Plane PIV Technique to Determine the Complete Velocity Gradient Tensor in a Turbulent Boundary Layer,” *Experiments in Fluids*, Vol. 39, No. 2, 2005, pp. 222–231. doi:10.1007/s00348-005-1019-z

[11] Guibert, P., and Lemoyne, L., “Dual Particle Image Velocimetry for Transient Flow Field Measurements,” *Experiments in Fluids*, Vol. 33, No. 2, 2002, pp. 355–367. doi:10.1007/s00348-002-0457-0

[12] Hu, H., Saga, T., Kobayashi, T., Taniguchi, N., and Yasuki, M., “Dualplane Stereoscopic Particle Image Velocimetry: System Set-Up and Its Application on a Lobed Jet Mixing Flow,” *Experiments in Fluids*, Vol. 31, No. 3, 2001, pp. 277–293. doi:10.1007/s003480100283

[13] Kähler, C. J., and Kompenhans, J., “Fundamentals of Multiple Plane Stereo Particle Image Velocimetry,” *Experiments in Fluids*, Vol. 29, No. 1, 2000, pp. S070–S077.

[14] Kähler, C. J., “Investigation of the Spatio-Temporal Flow Structure in the Buffer Region of a Turbulent Boundary Layer by Means of Multiple Plane Stereo PIV,” *Experiments in Fluids*, Vol. 36, No. 1, 2004, pp. 114–130. doi:10.1007/s00348-003-0680-3

[15] Mullin, J. A., and Dahm, W. J. A., “Dual-Plane Stereo Particle Image Velocimetry (DSPIV) for Measuring Velocity Gradient Fields at Intermediate and Small Scales of Turbulent Flows,” *Experiments in Fluids*, Vol. 38, No. 2, 2005, pp. 185–196. doi:10.1007/s00348-004-0898-8

[16] Souverein, L. J., van Oudheusden, B. W., Scarano, F., and Dupont, P., “Application of a Dual-Plane Particle Image Velocimetry (Dual-PIV) Technique for the Unsteadiness Characterization of a Shock Wave Turbulent Boundary Layer Interaction,” *Measurement Science and Technology*, Vol. 20, No. 7, 2009, Paper 074003. doi:10.1088/0957-0233/20/7/074003

[17] Garnier, E., Sagaut, P., and Deville, M., “Large-Eddy Simulation of the Shock/Boundary Layer Interaction,” *AIAA Journal*, Vol. 40, No. 10, 2002, pp. 1935–1944. doi:10.2514/2.1552

[18] Agostini, L., Larchevêque, L., Dupont, P., Debiève, J.-F., and Dussauge, J.-P., “Zones of Influence and Shock Motion in a Shock/Boundary-Layer Interaction,” *AIAA Journal*, Vol. 50, No. 6, 2012, pp. 1377–1387. doi:10.2514/1.J051516

[19] Touber, E., and Sandham, N. D., “Low-Order Stochastic Modelling of Low-Frequency Motions in Reflected Shock-Wave/Boundary-Layer Interactions,” *Journal of Fluid Mechanics*, Vol. 671, March 2011, pp. 417–465. doi:10.1017/S0022112010005811

[20] Riou, J., Garnier, E., and Basdevant, C., “Compressibility Effects on the Vortical Flow over a 65° Sweep Delta Wing,” *Physics of Fluids*, Vol. 22, No. 3, 2010, Paper 035102. doi:10.1063/1.3327286

[21] Simon, F., Deck, S., Guillen, P., Sagaut, P., and Merlen, A., “Numerical Simulation of the Compressible Mixing Layer Past an Axisymmetric Trailing Edge,” *Journal of Fluid Mechanics*, Vol. 591, Nov. 2007, pp. 215–253. doi:10.1017/S0022112007008129

[22] Garnier, E., “Stimulated Detached Eddy Simulation of Three-Dimensional Shock/Boundary Layer Interaction,” *Shock Waves*, Vol. 19, No. 6, 2009, pp. 479–486. doi:10.1007/s00193-009-0233-7

[23] Roe, P. L., “Approximate Riemann Solvers, Parameter Vectors, and Difference Schemes,” *Journal of Computational Physics*, Vol. 43, No. 2, 1981, pp. 357–372. doi:10.1016/0021-9991(81)90128-5

[24] Ducros, F., Ferrand, V., Nicoud, F., Weber, C., Darracq, D., Gacherieu, C., and Poinsot, T., “Large-Eddy Simulation of the Shock/Turbulence Interaction,” *Journal of Computational Physics*, Vol. 152, No. 2, 1999, pp. 517–549. doi:10.1006/jcph.1999.6238

[25] Lenormand, E., Sagaut, P., Ta Phuoc, L., and Comte, P., “Subgrid-Scale Models for Large-Eddy Simulation of Compressible Wall Bounded

Flows," *AIAA Journal*, Vol. 38, No. 8, 2000, pp. 1340–1350.
doi:10.2514/2.1133

[26] Gear, C. W., *Gear, Numerical Initial Value Problems in Ordinary Differential Equations*, Prentice–Hall, Upper Saddle River, NJ, 1971, pp. 209–223.

[27] Morgan, B., Duraisamy, K., Nguyen, N., Kawai, S., and Lele, S. K., "Flow Physics and RANS Modelling of Oblique Shock/Turbulent Boundary Layer Interaction," *Journal of Fluid Mechanics*, Vol. 729, Aug. 2013, pp. 231–284.
doi:10.1017/jfm.2013.301

[28] Wu, M., and Pino Martin, M., "Analysis of Shock Motion in Shockwave and Turbulent Boundary Layer Interaction Using Direct Numerical Simulation Data," *Journal of Fluid Mechanics*, Vol. 594, Jan. 2008, pp. 71–83.
doi:10.1017/S0022112007009044

[29] Agostini, L., Larchevêque, L., and Dupont, P., "Mechanism of Shock Unsteadiness in Separated Shock/Boundary-Layer Interactions," *Physics of Fluids*, Vol. 27, No. 12, 2015, Paper 126103.
doi:10.1063/1.4937350

[30] Wang, B., Sandham, N. D., Hu, Z., and Liu, W., "Numerical Study of Oblique Shock-Wave/Boundary-Layer Interaction Considering Sidewall Effects," *Journal of Fluid Mechanics*, Vol. 767, March 2015, pp. 526–561.
doi:10.1017/jfm.2015.58

[31] Dussauge, J. P., Dupont, P., and Debiève, J.-F., "Unsteadiness in Shock Wave Boundary Layer Interactions with Separation," *Aerospace Science and Technology*, Vol. 10, No. 2, 2006, pp. 85–91.
doi:10.1016/j.ast.2005.09.006

[32] Ganapathisubramani, B., Clemens, N. T., and Dolling, D. S., "Low-Frequency Dynamics of Shock-Induced Separation in a Compression Ramp Interaction," *Journal of Fluid Mechanics*, Vol. 636, Oct. 2009, pp. 397–425.
doi:10.1017/S0022112009007952

[33] Piponniau, S., Dussauge, J.-P., Debiève, J.-F., and Dupont, P., "A Simple Model for Low-Frequency Unsteadiness in Shock-Induced Separation," *Journal of Fluid Mechanics*, Vol. 629, June 2009, pp. 87–108.
doi:10.1017/S0022112009006417

[34] Priebe, S., and Pino Martin, M., "Low-Frequency Unsteadiness in Shock Wave–Turbulent Boundary Layer Interaction," *Journal of Fluid Mechanics*, Vol. 699, May 2012, pp. 1–49.
doi:10.1017/jfm.2011.560

[35] Touber, E., and Sandham, N. D., "Large-Eddy Simulation of Low-Frequency Unsteadiness in a Turbulent Shock-Induced Separation Bubble," *Theoretical and Computational Fluid Dynamics*, Vol. 23, No. 2, 2009, pp. 79–107.
doi:10.1007/s00162-009-0103-z

[36] Dussauge, J. P., and Piponniau, S., "Shock/Boundary-Layer Interactions: Possible Sources of Unsteadiness," *Journal of Fluids and Structures*, Vol. 24, No. 8, 2008, pp. 1166–1175.
doi:10.1016/j.jfluidstructs.2008.06.003

J. Poggie
*Associate Editor*